First-principles study of lattice instabilities in ferromagnetic Ni_2MnGa

Claudia Bungaro* and K. M. Rabe
Department of Physics and Astronomy, Rutgers University, Piscataway, New Jersey 08854-8019, USA

A. Dal Corso
Scuola Internazionale Superiore di Studi Avanzati (SISSA), Via Beirut 2/4, 34014 Trieste, Italy
(Received 20 March 2003; revised manuscript received 19 June 2003; published 8 October 2003)

The phonon-dispersion relations and elastic constants for ferromagnetic Ni_2MnGa in the cubic and tetragonally distorted Heusler structures are computed using density-functional and density-functional-perturbation theory within the spin-polarized generalized-gradient approximation. For $0.9<c/a<1.06$, the TA_2 transverse-acoustic branch along [110] and the symmetry-related directions exhibit a dynamical instability at a wave vector that depends on c/a. Through examination of the Fermi-surface nesting and electron-phonon coupling, this is identified as a Kohn anomaly. In the parent cubic phase the computed tetragonal shear elastic constant, $C'=(C_{11}-C_{12})/2$, is close to zero, indicating a marginal elastic instability towards a uniform tetragonal distortion. We conclude that the cubic Heusler structure is unstable against a family of energy-lowering distortions produced by the coupling between a uniform tetragonal distortion and the corresponding [110] modulation. The computed relation between the c/a ratio and the modulation wave vector is in excellent agreement with structural data on the premartensitic ($c/a=1$) and martensitic ($c/a=0.94$) phases of Ni_2MnGa.

DOI: 10.1103/PhysRevB.68.134104 PACS number(s): 64.70.Kb, 63.20.Dj, 31.15.Ar, 75.50.Cc

I. INTRODUCTION

Ferromagnetic shape-memory alloys displaying large magnetic-field-induced strain have recently emerged as a new class of active materials, very promising for actuator and sensor applications. The largest known magnetostrain effects have been observed in Ni_2MnGa-based Heusler alloys, where up to 6% and 9.5% strains have been induced by a magnetic field less than 1 T.[1,2]

The magnetic shape-memory behavior is closely linked to the occurrence of a martensitic transformation in conjunction with a strong magnetocrystalline anisotropy of the low-temperature martensitic phase. For a deeper understanding of the magnetic shape-memory mechanism, a microscopic explanation for the origin of the martensitic transformation and the magnetocrystalline anisotropy is clearly needed. Towards this goal, we have used *ab initio* techniques to investigate the origin of the martensitic transformation.

Ni_2MnGa is the most intensively studied of the relatively few known ferromagnetic shape-memory materials. A number of thermal and stress-induced martensitic transformations have been observed in Ni_2MnGa-based alloys, and both transition temperatures and crystallographic structures are quite sensitive to alloy composition.

In the stoichiometric alloy Ni_2MnGa, which is ferromagnetic below $T_C \approx 380$ K, two thermally induced phase transitions have been observed. From the high-temperature cubic Heusler structure, a premartensitic phase transformation to a modulated cubic structure occurs below $T_{PM} \approx 260$ K,[3,4] followed by a martensitic transformation to a modulated tetragonal structure below $T_M \approx 220$ K.[5] The low-temperature martensitic phase has a tetragonal structure ($c/a=0.94$, $a=5.90$ Å) with a superimposed incommensurate modulation along the [110] direction, consisting of a shuffling of (110) planes in the $[\bar{1}10]$ direction with a periodicity of almost five interplanar distances, which corresponds to a wave vector $\mathbf{q}_M \approx (2\pi/a)(0.43, 0.43, 0)$ (Refs. 4,6). The low-temperature martensitic phase has a high magnetocrystalline anisotropy,[7] making it useful for applications. At a phenomenological level, the coupling between strain, modulation, and magnetization has recently been described in a Landau-theory framework.[8]

Some clues to the microscopic origin of the martensitic transitions are provided by the softening of particular phonons and elastic constants. Inelastic neutron-scattering experiments on the high-temperature phase found a significant, though incomplete, softening in the TA_2 phonon branch along the [110] direction, at a wave vector $\mathbf{q}_{PM} \approx (2\pi/a)$ (0.33, 0.33, 0) (Ref. 3). The phonon softening has been found to correspond to a premartensitic phase occurring between the high-temperature cubic and low-temperature martensitic structures. The premartensitic phase has a cubic structure with a superimposed [110]-transverse shuffling modulation, analogous to the modulation of the martensitic phase but with a different periodicity of almost six interplanar distances.[3] While the PM phase is anticipated by a precursor phonon softening at $\mathbf{q}_{PM}$, no phonon softening at $\mathbf{q}_M$ has been observed above T_M.

The aim of this study is to provide a unified explanation for the microscopic origin of the rich variety of phase transitions and modulated structures occurring in this ferromagnetic shape-memory alloy. To this end we have performed a first-principles study of the phonon dispersion of cubic ferromagnetic Ni_2MnGa and its dependence on uniform tetragonal strain. The presence of unstable phonons and anomalously low elastic constants in these high-symmetry reference structures is taken as predictive of phase transitions to low-temperature distorted Heusler structures and strong

temperature dependence for these quantities. In our calculations we use the spin-polarized generalized-gradient approximation (σ-GGA) recently developed within the density-functional-perturbation theory (DFPT) formalism.[9] This approach allows us to obtain an accurate description of the structural, magnetic, and vibrational properties of Ni_2MnGa.

The paper is organized as follows. The details of the computational method are given in Sec. II. In Sec. III we present the results for the cubic Heusler structure. The crystal structure and magnetization are discussed in Sec. III A. Sec. III B is devoted to the phonon dispersion, with particular attention to the phonon anomaly and related dynamical instability. The origin of the phonon anomaly is discussed in Sec. III C. The computed elastic constants are presented and discussed in Sec. III D. In Sec. IV we investigate the dependence of the phonon dispersions and lattice instabilities on uniform tetragonal strain. In Sec. V the main results are summarized and the microscopic origin of the observed phase transitions explained.

II. COMPUTATIONAL METHOD

Our calculations have been performed within the framework of density-functional and density-functional-perturbation theory. In particular, the vibrational properties have been computed using a recent implementation of ultrasoft pseudopotentials into DFPT.[10] Pseudopotentials were used to describe the interaction between ionic cores and valence electrons. For Ni and Mn we used ultrasoft pseudopotentials[11] that were generated as described in Refs. 12,13, respectively, using as reference configurations the all-electron atomic configurations $[\mathrm{Ne}]3s_2 3p_6 3d_9 4s_1$, for Ni, and $[\mathrm{Ne}]3s_2 3p_6 3d_5 4s_2$, for Mn. The $3s$ and $3p$ electrons were frozen in the core while $3d$ and $4s$ were included in the valence. The scattering properties in the range of energies of the occupied states and of the empty $4p$ states of Ni and Mn were accurately reproduced by construction. The nonlinear core correction is used to account for the overlap between the core and the valence charges.[14] For the Ga atom we used a norm-conserving pseudopotential, which also includes a nonlinear core correction, treating the $4s$ and $4p$ states as valence levels. To describe the effects of exchange and correlation, we used the Perdew-Burke-Ernzerhof[15] functional with the spin-polarized generalized-gradient correction, recently implemented within the DFPT formalism in the PWSCF code.[9] For comparison, we have performed calculations within the local spin-density approximation (LSDA) using the Perdew-Zunger parametrization of the exchange and correlation energy. The plane-wave basis set had a kinetic-energy cutoff of 25 Ry. The augmentation charges, required by the use of ultrasoft pseudopotentials, were expanded with an energy cutoff of 450 Ry. The Brillouin-zone integration was performed using the smearing technique,[16] suitable for metallic systems. The structural properties and most of the phonon frequencies are well converged using a first-order smearing function with a smearing parameter $\sigma = 0.03$ Ry and a fcc (6, 6, 6) Monkhorst-Pack grid,[17] yielding 28 **k** points in the irreducible wedge of the Brillouin zone (IBZ) for the cubic structure. To obtain an accurate description of the anomalous TA_2 phonon branch, a smaller smearing parameter is necessary and, consequently, a finer **k** point sampling. An accuracy to within a few cm^{-1} has been obtained using $\sigma = 0.01$ Ry and a fcc (10, 10, 10) **K** point grid, yielding 110 **k** points in the IBZ, for the cubic structure. For the tetragonal structure, an (8, 8, 8) **k** point grid yielding 144 **k** points in the IBZ of the face-centered orthorhombic unit cell was used.

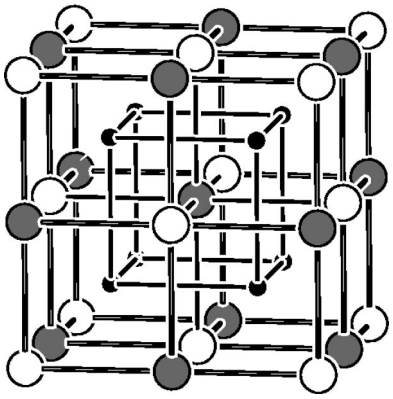

FIG. 1. The fcc $L2_1$ Heusler structure of Ni_2MnGa. The small circles, large open circles, and large filled circles represent Ni, Mn, and Ga, respectively.

We studied the lattice-dynamical properties using DFPT with which the dynamical matrix at any **q** point in the Brillouin zone (BZ) can be directly computed (see Ref. 18 for full details). To compute the full phonon dispersions of the cubic structure, we computed the interatomic force constants by Fourier transformation of the dynamical matrices computed on a (6, 6, 6) **q** point grid in the fcc BZ. The phonon dispersions along the [110] ([011]) direction was obtained by interpolating the dynamical matrices computed on a finer mesh of 24 **q** points between Γ and the shortest reciprocal-space vector parallel to the [110] ([011]) direction. An even denser mesh of **q** points has been used in the proximity of the anomaly for a more accurate interpolation of the TA_2 branch.

III. CUBIC Ni_2MnGa

In this section, we report the results of calculations for Ni_2MnGa in the fcc $L2_1$ Heusler structure (see Fig. 1).

A. Crystal structure and magnetization

In Table I we give the minimum-energy lattice parameter a_0, the bulk modulus B_0, and the magnetic moment per unit cell μ_0 computed within the spin-polarized σ-GGA. Note that to obtain convergence to within $0.01\mu_B$, μ_0 has been computed on a (10, 10, 10) **k**-point grid with $\sigma = 0.01$ Ry. These results agree well with those of all-electron calculations (FLAPW) performed using the σ-GGA.[19] The theoretical results are also in very good agreement with the experimental data; the theoretical lattice parameter obtained with σ-GGA is equal, within theoretical precision, to the experimental value. For comparison, the LSDA results are included in Table I. The LSDA lattice parameter is 2.5% smaller than

TABLE I. Equilibrium lattice parameter a_0, bulk modulus B_0, and magnetic moment μ_0 for Ni_2MnGa in the $L2_1$ Heusler structure. Calculations using the spin-polarized GGA (σ-GGA) are compared with experimental data and with the results obtained using LSDA.

	a_0(a.u.)	B_0 (Mbar)	$\mu_0(\mu_B)$
σ-GGA	11.03	155	4.27
LSDA	10.74	202	3.92
FLAPW-σ-GGA[a]	10.98	156	4.09
Expt.	11.01[b]	146[c]	4.17[b]

[a]Reference 32.
[b]Reference 27.
[c]Reference 19.

the experimental value. This underestimate of the lattice parameter is correlated with an increase in the bulk modulus to 38% higher than the experimental value.

Our calculated electronic density of states (not shown) is in good agreement with the density of states of Ref. 20.

B. Phonon dispersion relation

The phonon dispersions of the ferromagnetic cubic structure ($a_0 = 11.03$ a.u.) have been computed, using σ-GGA, for $\vec{q}$ along high-symmetry lines in the first Brillouin zone, as shown in Fig. 2. The solid lines indicate the computed phonon dispersion converged to within a few wave numbers. The theoretical phonon-dispersion curves are in excellent agreement with the available inelastic neutron scattering-data.[4,21]

To evaluate the accuracy of the theoretical method, the phonon frequencies computed using different approximations for the exchange and correlation energy, at the zone boundary X point, are given in Table II. Since the experimental frequency of the anomalous $(\zeta\zeta 0)$-acoustic branch is not strongly temperature dependent at this **q** point, it is a good reference for evaluating the accuracy of the theoretical method. The experimental frequency for the transverse-acoustic mode X_5' is in very good agreement with the phonon frequency computed using the σ-GGA, with the computed value being about 6% softer. For comparison, we have also done the computation with LSDA. Calculations for the cubic structure with the LSDA lattice constant yield frequencies about 10% harder than those computed using the σ-GGA, except for the lowest X_5' mode which is 7% softer, increasing the discrepancy with experiment. In addition, the ordering of the modes in LSDA is different. Specifically, the X_4' mode is softer than the nearby X_5' and X_5 modes. We have also computed the phonon frequencies within the LSDA but fixing the lattice parameter to the equilibrium value computed in the σ-GGA. The result is that all the modes soften, so that the frequencies are about 10% smaller than those calculated with σ-GGA. This softening results in an even greater discrepancy with the experimental X_5' mode (20%). We conclude that the better accuracy of σ-GGA is not merely an effect of the more accurate value of the equilibrium lattice parameter. All calculations reported below were performed with σ-GGA.

TABLE II. Phonon frequencies (in cm^{-1}) computed at the zone-boundary point X. Results obtained using different approximations for the exchange and correlation energy, σ-GGA and LSDA, are compared with the experiment.

a_0	σ-GGA $a_0(\sigma$-GGA)	LSDA a_0(LSDA)	LSDA $a_0(\sigma$-GGA)	Expt.
X_5'	82	76	70	87
X_1'	160	179	151	
X_5	174	191	161	
X_5'	176	195	166	
X_4'	178	185	159	
X_1	191	203	168	
X_1'	227	249	212	
X_5'	259	286	233	

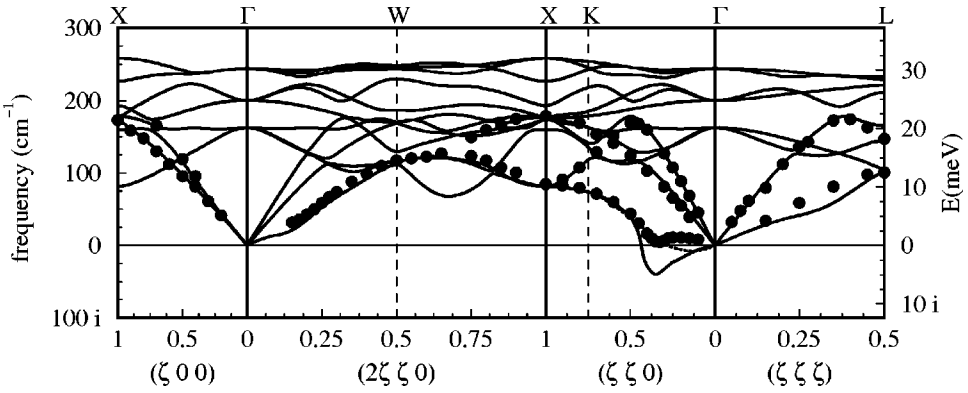

FIG. 2. Full phonon dispersion of ferromagnetic Ni_2MnGa in the fcc Heusler structure, along high-symmetry lines of the fcc BZ. Solid lines are fully converged *ab initio* calculations obtained using an effective electronic temperature $\sigma = 0.01$ Ry. The dashed line is the dispersion obtained using a higher effective electronic temperature, $\sigma = 0.03$ Ry showing the dependence of the anomaly in the lowest acoustic branch along the $(\zeta\zeta 0)$ direction on the effective electronic temperature. The circles indicate the neutron-scattering data from Refs. 4, 21. The imaginary values of phonon frequencies are plotted along the negative frequency axis. The wave vector coordinate ζ is in units of $(2\pi/a)$.

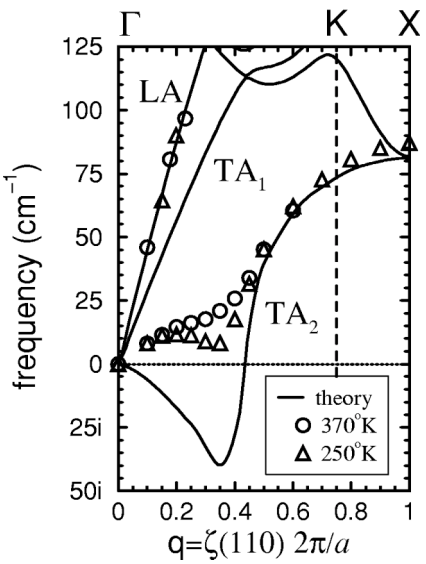

FIG. 3. Partial phonon dispersion of Ni_2MnGa in the fcc Heusler structure, along the Γ-K-X line in the [110] direction. The theoretical data are the same as in Fig. 2. The experimental data taken at 250 K and 270 K are shown for comparison.

The most striking feature of the phonon-dispersion relation in Fig. 2 is the anomalous dip in the lowest branch of the transverse-acoustic modes (TA_2) along [110]. The minimum at the incommensurate wave vector $\mathbf{q}_0=(2\pi/a)(\zeta_0,\ \zeta_0,0)$, with $\zeta_0=0.34$, is at imaginary frequency. Thus, the crystal is dynamically unstable to the lattice distortion corresponding to the eigenvector of this mode, which consists of a nearly rigid displacement of the (110) atomic planes along the $[1\bar{1}0]$ direction with a modulation period of slightly less than six interplanar distances along the [110] direction. This energy-lowering distortion can be specified by an amplitude $\mathbf{u}$ and a phase, ϕ:

$$\mathbf{u}_m=\mathbf{u}\cos(m\zeta_0\pi+\phi), \tag{1}$$

where $\mathbf{u}_m$ is the displacement of the mth (110) atomic plane along the $[1\bar{1}0]$ direction. Due to the cubic symmetry, there are 12 equivalent anomalies along the $\langle 110\rangle$ directions which give rise to six different but crystallographically equivalent lattice modulations $\mathbf{u}_m$.

The phonon anomaly is shown in more detail in Fig. 3, where the theoretical dispersion is compared with inelastic neutron-scattering data taken at two different temperatures: $T=370$ K (squares) and $T=250$ K (triangles).[3] The experimental data display an anomaly in the TA_2 branch, which corresponds to the anomaly predicted by our theoretical dispersion. The wave vector of the experimentally observed anomaly is $\zeta_{PM}\approx 0.33$,[3] in excellent agreement with the theoretical value. For those modes that do not have a strong dependence upon temperature, such as the LA branch and the TA_2 modes away from the anomaly ($\zeta\geqslant 0.45$), the agreement between theory and experiment is very good. To compare theory and experiment for modes that are strongly temperature dependent, we need to extrapolate the experimental values to $T=0$ K. In accordance with the soft-mode theory,

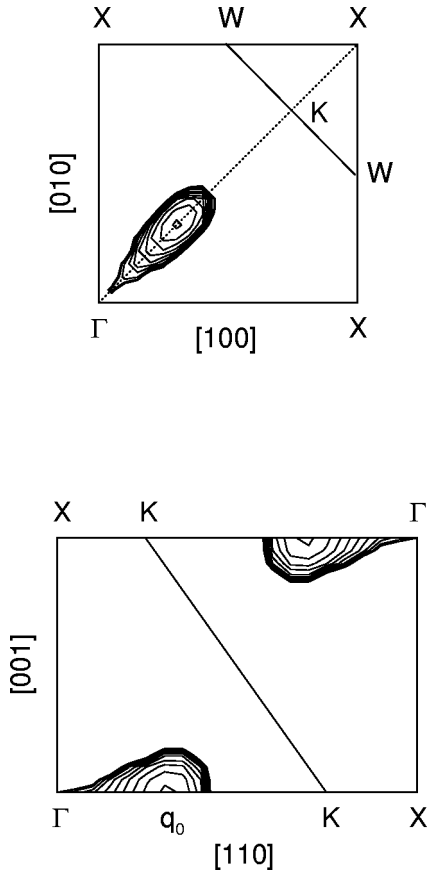

FIG. 4. Contour plots of the imaginary phonon frequencies in the (001) plane (a) and $(1\bar{1}0)$ plane (b) of the fcc BZ. These contour plots show the region in $\mathbf{q}$ space where the crystal is dynamically unstable. This occurs in a narrow valley situated along the [110] direction with its minimum at the critical wave vector $\mathbf{q}_0=(0.34,0.34,0)$.

$(\hbar\omega)^2$ is experimentally observed to decrease linearly with temperature above $T_{PM}=260$ K. Extrapolation to $T=0$ K gives an imaginary frequency of $30i$ cm^{-1}, which is in reasonable agreement with the computed value.

Examination of the phonon dispersion throughout the entire BZ shows that imaginary frequencies leading to dynamical instabilities occur only in a very localized region in $\mathbf{q}$ space. This is in agreement with the experimental dispersion measured in the direction perpendicular to $\mathbf{q}_0$, $\mathbf{q}=\mathbf{q}_0+(\zeta,-\zeta,0)$.[4] The contour plot in Fig. 4 shows that the lattice instability is confined to a "drop-shaped" small region in reciprocal space, located along the [110] direction and centered at the critical wave vector $\mathbf{q}_0$, where the dominant instability occurs. The localized nature of the anomaly in $\mathbf{q}$ space is a signature of its electronic origin, as will be discussed in detail in the following section.

C. Origin of the anomaly

Screening due to electron-phonon coupling involving electronic states near the Fermi level in metals can give rise to anomalous dips in the phonon dispersion, called Kohn anomalies. The occurrence of these anomalies depends

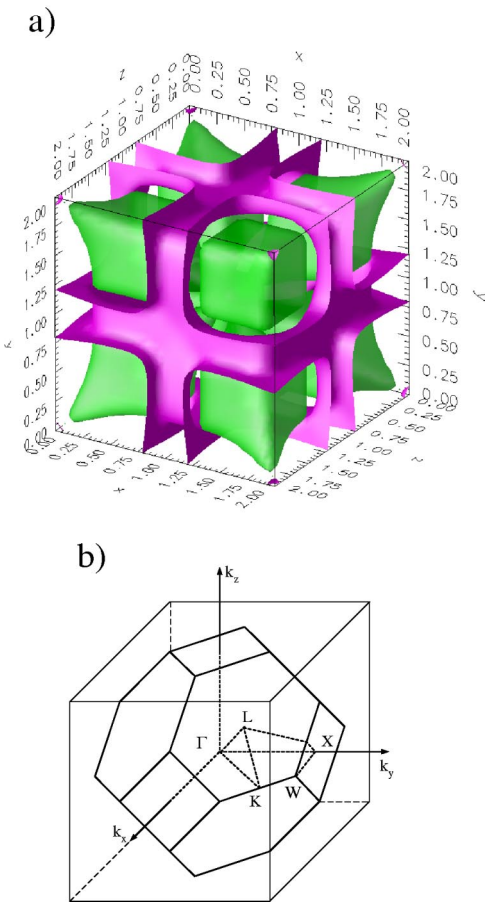

FIG. 5. (Color online only) (a) Fermi surface of the minority-spin bands for cubic Ni_2MnGa. (b) The fcc BZ inscribed in the same cube as in (a) is shown as a reference. k_x, k_y, k_z, are in units of $2\pi/a$.

mainly on the geometry of the Fermi surface, as well as on the **q** dependence of electron-phonon matrix elements. If the Fermi surface has flat portions with nesting vector $\mathbf{q}_0$, there generally will be very strong screening of the potential perturbation due to atomic displacements at that wave vector, leading to a pronounced softening highly localized in **q** space. The effect of Fermi-surface geometry can be quantified by calculation of the generalized susceptibility, as in Refs. 22, 23.

In cubic Ni_2MnGa, the Fermi level crosses both minority- and majority-spin bands. Of the two Fermi surfaces, only the one for the minority-spin bands, plotted in Fig. 5, shows obvious nesting features. In particular, they exhibit nesting features which are consistent with the anomaly in our phonon dispersion which, in turn, is in very good agreement with the experiments. In Fig. 6 we show two cross sections of the minority-spin Fermi surface and examples of nesting with vector $\mathbf{q}_0=0.34(1,1,0)$. The shape of our Fermi surface agrees with those of Refs. 22, 23. There are however small quantitative differences that result in a different nesting vector and position of the peak in the generalized susceptibility. We have carefully investigated the possibility that these differences may be related to **k**-point sampling. In order to describe details of the Fermi-surface structure, it is necessary to use a very high density of **k** points. Since the anomalous frequency is extremely sensitive to the Fermi-surface nesting, it provides the natural measure of convergence for the calculation. We checked convergence of the anomalous frequency with respect to **k**-point mesh and broadening (see Table III). We find full convergence only at a **k**-point density significantly higher than that used in the calculations of Refs. 22, 23. Other possible sources of difference between the calculations could be the choice of lattice parameter (we have used the optimized theoretical lattice constant, which is also in good agreement with experiment) or of the exchange-correlation functional. [110] appears to be a direction for which the anomaly is strongest. For example, although there is nesting along [100] as well, there is no sign of an anomaly in the phonon dispersion. This can be attributed to the vanishing of the relevant electron-phonon matrix elements.

The strength of a Kohn anomaly is expected to be very sensitive to electronic temperature, with an increasing temperature reducing the sharpness of the Fermi surface and thus weakening the anomaly. In our calculations, the sensitivity to electronic temperature can be directly investigated, as the smearing parameter σ plays the role of a fictitious electronic temperature. In Table III we show the dependence on σ of those modes at the critical wave vector $\mathbf{q}_0$ that have the same symmetry as the soft TA_2 branch (i.e., the three modes of Σ_3 symmetry). The anomalous TA_2 mode $\Sigma_3(1)$ is much more sensitive to the fictitious electronic temperature than the other two modes. All the frequencies are well converged for $\sigma=0.01$ Ry. The dependence of the phonon anomaly upon the electronic temperature is also shown in Fig. 2, where the dispersion of the anomalous TA_2 branch computed with $\sigma=0.03$ Ry (dashed line) is compared with the fully converged calculation for $\sigma=0.01$ Ry (solid line). Only the modes with wave vectors close to the anomaly, $(\zeta_0-0.16)<\zeta<(\zeta_0+0.16)$, are affected by the change in the electronic temperature. The anomaly is smoothed out as the fictitious electronic temperature is increased. Thus, we conclude that the computed dip is indeed a Kohn anomaly.

D. Elastic constants

The computed elastic constants for the ferromagnetic cubic structure are reported in Table IV. In a first-principles framework, the standard approach for obtaining elastic constants is to compute the stress tensor for a selected set of small strains. The computation of the stress tensor is performed using the formalism of Nielsen and Martin,[24] which is a standard feature of the PWSCF code.[25] To obtain convergence at the level of a few GPa, we have used very dense **k** point meshes [up to (14 14 14), corresponding to 10 976 points in the BZ]. To compute C_{11} and C_{12} the cubic crystal is distorted by the tetragonal deformation: $\epsilon_{zz}=\epsilon$, $\epsilon_{xx}=\epsilon_{yy}=0$. For small deformations the stress σ_{ij} is linear with ϵ: $\sigma_{xx}=\sigma_{yy}=C_{12}\epsilon$, and $\sigma_{zz}=C_{11}\epsilon$. The values so obtained for the elastic constants C_{11}, C_{12}, and the shear modulus $C'=(C_{11}-C_{12})/2$ are indicated as "theory 1" in Table IV.

The small magnitude of C' requires additional attention. We performed an independent computation by considering the tetragonal deformation $\epsilon_{xx}=\epsilon_{yy}=\epsilon$, $\epsilon_{zz}=-2\epsilon$. For

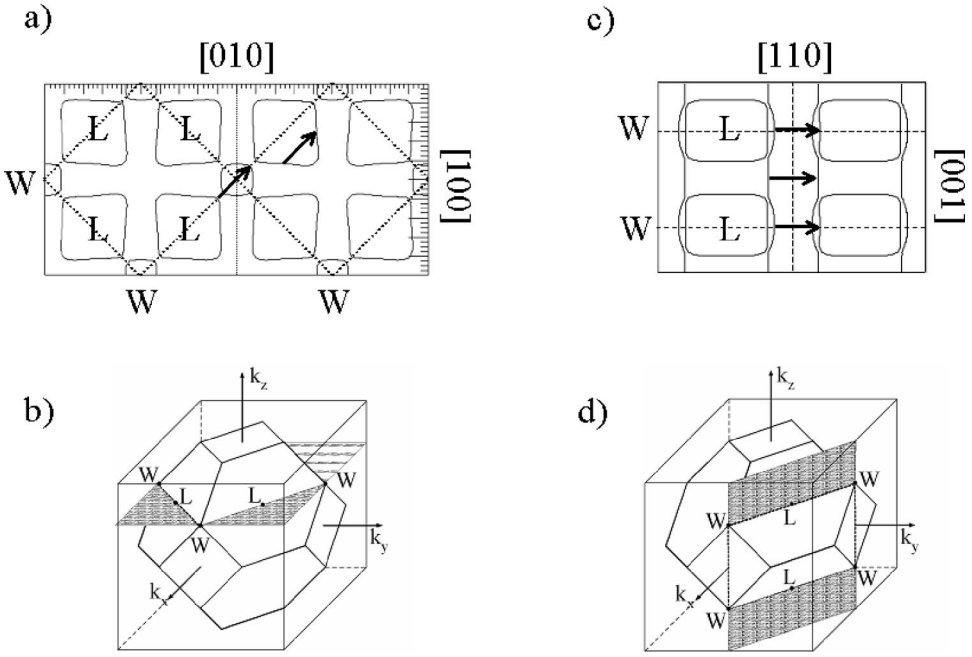

FIG. 6. Cross section of the minority-spin Fermi surface (a) with the (001) plane $k_z=0.5$ [shown in (b)], and (c) with the (110) plane $k_x+k_y=1$ [shown in (d)]. The arrows are examples of nesting vectors $\mathbf{q}_0=0.34(1,1,0)$.

small ϵ we have that $\sigma_{xx}=\sigma_{yy}=2C'\epsilon$ and $\sigma_{zz}=-4C'\epsilon$. This direct calculation gives $C'=(2\pm2)$ GPa, in good agreement with the value obtained as a difference of C_{11} and C_{12} in theory 1. The near-zero value of C' implies that there is almost no energy cost for a small tetragonal shear distortion of the type $2\epsilon_{xx}=2\epsilon_{yy}=-\epsilon_{zz}$. Evidence of this marginal elastic instability towards small volume-preserving tetragonal distortions was also found in Ref. 26, where it was shown that the energy surface as a function of c/a is remarkably flat; specifically, the change in energy associated with varying the c/a ratio in the range of values between 0.97 and 1.01 is almost zero to within numerical accuracy.

In Table IV (theory 2) we also show the values of the elastic constants estimated from the slope of the long wavelength acoustic modes along the [110] direction. The elastic constants C_{44}, C', and $C_L=(C_{11}+C_{12}+2C_{44})/2$ correspond to the TA_1, TA_2, and LA modes, respectively. These determine the values of C_{11} and C_{12} given in the table. The evaluation of the elastic constants from the phonon dispersion is less accurate, especially for C′ where the corresponding TA_2 branch deviates from a linear behavior already at very small **q**.

These elastic constants have been computed for the unstable (and therefore hypothetical) cubic Heusler structure at zero temperature, and caution must be exercised in attempting to compare these values with experiment. In the case of elastic constants for which the observed temperature dependence is slight, we expect a reasonable comparison between the computed values and the measurements. The elastic constants in the high-temperature cubic phase have been experimentally determined between room temperature and the intermediate premartensitic phase transition by measuring the velocity of ultrasonic waves.[27,28] These experiments show that the elastic constants C_L and C_{11} are almost temperature independent. As expected, we indeed find good agreement between theory and room temperature measurements for C_L and C_{11}. In contrast, the transverse elastic constants C_{44} and C' exhibit strong temperature dependence, softening as the premartensitic phase-transition temperature is approached. While the softening is small for C_{44}, it is more dramatic for C', which decreases by 60% from room temperature to the transition. Although we cannot predict the detailed behavior from our $T=0$ calculation, the strong temperature dependence is consistent with the anomalous near-zero value for C'.

TABLE III. Dependence upon the smearing parameter σ of the frequency of the three Σ_3 modes at the critical wave vector $\mathbf{q}_0$. The $\Sigma_3(1)$ mode is the anomalous TA_2 mode, the other two, $\Sigma_3(2)$ and $\Sigma_3(3)$, are higher-frequency optical modes. The **k**-point mesh needed to achieve convergence for each of the values of σ is also reported. Frequencies are in cm^{-1}.

σ(Ry)	**k** mesh	$\Sigma_3(1)$	$\Sigma_3(2)$	$\Sigma_3(3)$
0.03	(6 6 6)	8	195	244
0.01	(10 10 10)	39*i*	195	242
0.005	(12 12 12)	39*i*	195	242

TABLE IV. Elastic constants, in GPa, for ferromagnetic Ni_2MnGa in the cubic Heusler structure. Theory 1, elastic constants from stress calculation under strain. Theory 2, elastic constants estimated from the slope of the $[\zeta\zeta 0]$ acoustic branches close to Γ: C', C_{44}, and C_L correspond to the TA_2, TA_1, and LA modes, respectively. Room-temperature measurements are shown for comparison.

	C_{11}	C_{12}	C'	C_{44}	C_L
Theory 1	153±2	148±2	2.5±2		
Theory 2	138±9	143±9	−2.5±5	100±5	240±5
Expt.	152	143	4.5	103	250
Expt.	136±3		22±2	102±3	222±9

[a]Reference 27.
[b]Reference 28.

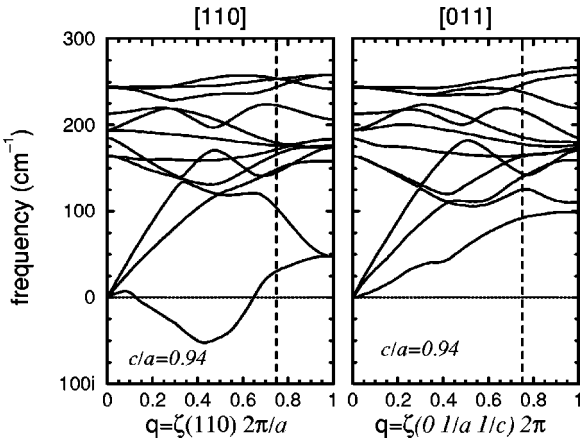

FIG. 7. *Ab initio* [110] and [011] phonon dispersions for ferromagnetic Ni_2MnGa in the tetragonal structure ($c/a=0.94$, $a=11.26$ a.u.).

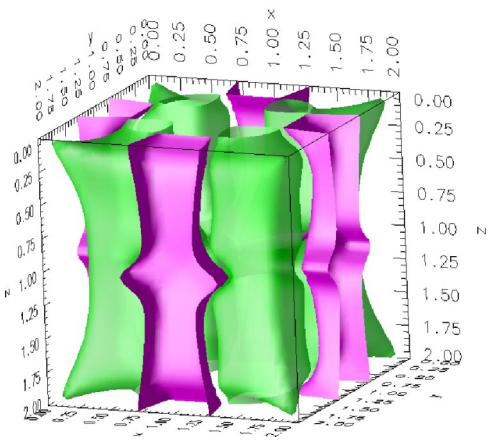

FIG. 8. (Color online only) Fermi surface of the minority-spin bands for tetragonal Ni_2MnGa ($c/a=0.94$).

IV. TETRAGONAL Ni_2MnGa

The identification of unstable phonons at $\mathbf{q}_0=(2\pi/a)\times(\zeta_0,\zeta_0,0)$, with $\zeta_0=0.34$, in the cubic Heusler structure leads naturally to an understanding of the transition to the premartensitic cubic-modulated phase with decreasing temperature. To explore the subsequent transition to the low-temperature martensitic phase with $c/a=0.94$ and modulation wave vector $\zeta_0=0.43$, we extended the calculations of phonon dispersion to Heusler structures with uniform volume-preserving tetragonal strains ranging from $c/a=0.88$ to $c/a=1.06$, with particular attention to the TA modes along the $\langle 110\rangle$ directions.

A. Tetragonal structure with $c/a=0.94$

We first consider in detail the volume-preserving tetragonal distortion with $c/a=0.94$, corresponding to the low-temperature martensitic phase. The phonon dispersions computed along the inequivalent [110] and [011] directions of the tetragonal BZ are shown in Fig. 7. The only mode substantially affected by the tetragonal distortion is the anomalous TA_2 mode. We find an overall softening (hardening) of the TA_2 branch in the [110] ([011]) direction. The anomaly is particularly affected by the tetragonal distortion. Along the $\langle 110\rangle$ directions, which are perpendicular to the c axis, the phonon anomaly is more pronounced and is shifted to a larger $\mathbf{q}$ vector ($\zeta=0.43$) than in the cubic structure. This wavevector is in excellent agreement with the long period modulation observed experimentally in the tetragonal martensitic phase. In contrast, along the $\langle 011\rangle$ directions, the anomaly has almost completely disappeared; the entire branch is stable and there is only a very small wiggle in the TA_2 branch.

As in the cubic phase, the anomaly can be associated with features of the Fermi surface. In Fig. 8 we show the minority-spin Fermi surface computed for Ni_2MnGa in the tetragonal structure. It is related to the Fermi surface of the cubic structure with two major differences: (i) There are no flat surfaces perpendicular to the (001) direction and (ii) The ''pipes'' running along the faces of the tetragonal BZ are wider than the corresponding features in the cubic Fermi surface. As a consequence of these changes, induced by the tetragonal distortion, there is significant nesting only in the $\langle 110\rangle$ directions perpendicular to the c axis and the edges of the pipes are nested by the larger ($\zeta\zeta 0$) critical wave vector, $\zeta=0.43$. This explains why in the tetragonal structure there are pronounced Kohn anomalies only in the $\langle 110\rangle$ directions, at a larger wave vector than in the cubic structure.

B. Evolution of phonon anomaly with tetragonal deformation

To understand better the lattice instabilities and related structural energetics of Ni_2MnGa, we studied the evolution of the TA_2 phonon anomaly with uniform volume-preserving tetragonal strain.

Studying the phonon dispersions of the cubic Heusler structure ($c/a=1$) and its tetragonal distortion with $c/a=0.94$, we have identified the existence of the unstable mode at $\zeta=0.34$ and $\zeta=0.43$, respectively, which explains the transitions to the premartensitic and martensitic phases with decreasing temperature. The fact that for the two tetragonal strains the soft mode is always the TA_2 mode but with a different wave vector suggests that the wave vector of the soft mode and the tetragonal strain are coupled. We therefore studied in more detail the dependence of ζ upon tetragonal strain.

The dispersion of the TA_2 branch along the [110] direction is shown in Fig. 9 for several values of the c/a ratio. An overall softening of the TA_2 branch is observed with decreasing c/a ratio. With compressive strain ($c/a<1$) the anomaly occurs at a larger ζ_0 than in the cubic structure, and becomes broader and more pronounced. For $c/a\lesssim 0.91$ the entire branch is unstable. With tensile strain ($c/a>1$) the anomaly shifts to a smaller ζ_0 and becomes less pronounced. The lattice instability is completely eliminated for $c/a\gtrsim 1.06$. This is in agreement with the experimental observation of no superimposed modulations in a stress-induced tetragonal phase with $c/a=1.18$.[29]

In Fig. 9, we have shown the TA_2 branch for several different values of c/a. For each of these values of c/a, we can find the value of the wave vector ζ_0 for which the imaginary frequency of the TA_2 branch has its minimum. This

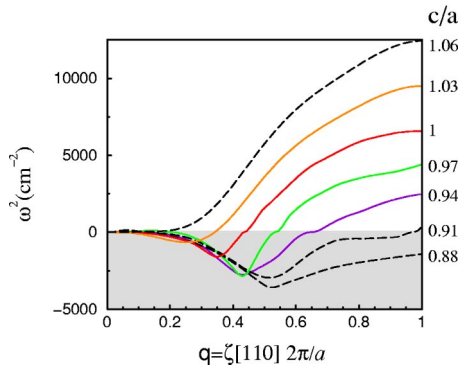

FIG. 9. (Color online only) Dispersion of the squared frequencies, for the anomalous TA_2 phonon branch, computed for different volume-preserving tetragonal distortions, with c/a ranging from 0.88 to 1.06.

gives us the dependence of the modulation wave vector upon strain and is shown in Fig. 10. Three regimes can be identified: (i) $c/a \lesssim 0.91$, where the entire TA_2 branch is unstable and there is no unique minimum; (ii) $0.9 < c/a < 1.06$, where the TA_2 branch displays a well-defined dynamical instability localized at the wave vector ζ_0 that depends on c/a; and (iii) $c/a \gtrsim 1.06$, where the lattice instability is completely eliminated and the TA_2 branch is stable over the whole BZ, so that no minimum is defined. Only in regime (ii) (Fig. 10) can a modulated structure be expected to occur.

In order to quantify these trends, in Fig. 11 we decompose the phonon frequency ω^2 into a short-range "normal" part ω_n^2 and a long-range "anomalous" part ω_a^2: $\omega^2(\zeta) = \omega_n^2(\zeta) + \omega_a^2(\zeta)$. The normal contribution, defined as $\omega_n^2(\zeta) = A[1 - \cos(\zeta\pi)]$, depends only upon short-range interatomic force constants and is connected to the local chemistry of the crystal. It corresponds to the simple model for the transverse $[1\bar{1}0]$ vibrations of the [110] planes when they interact only with a first-neighbor interplanar force constant: $K = -Am/2$, where m is the mass associated with each plane. The long-range anomalous contribution ω_a^2 depends on electronic screening effects that can be strongly **q** dependent. To fit the constant A in the definition of $\omega_n^2(\zeta)$, we assume that for $\zeta = 1$ the anomalous contribution is zero.

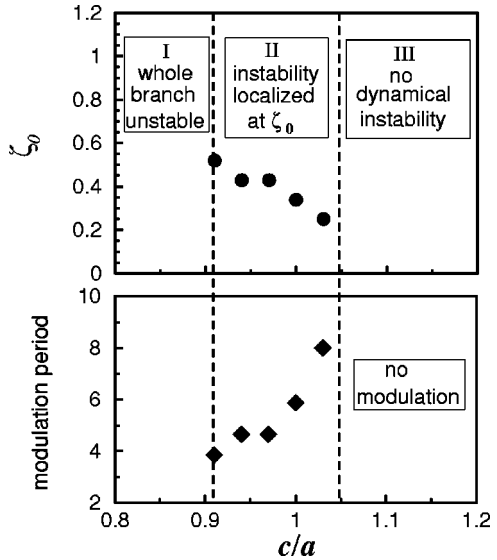

FIG. 10. Dependence upon c/a of the modulation wave vector ζ_0 and the related modulation period [in unit of (110) interplanar distances].

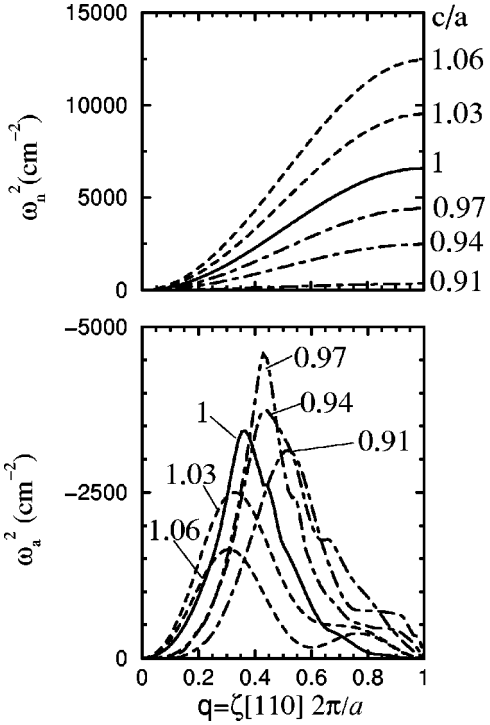

FIG. 11. Decomposition of ω^2 into "normal" (ω_n^2) and anomalous (ω_a^2) parts for different volume-preserving tetragonal distortions, with c/a varying from 0.91 to 1.06. Dashed lines are for $c/a > 1$, dot-dashed lines are for $c/a < 1$, and solid lines are for $c/a = 1$.

The short-range contribution softens with decreasing c/a ratio, causing the overall softening observed for the TA_2 branch. Decreasing c/a corresponds to a volume-preserving tetragonal distortion with a shorter c and larger a. Therefore smaller c/a values correspond to a larger [110] interplanar distance, which leads to a weaker interplanar force constant and therefore a softer ω_n^2.

The anomalous contribution ω_a^2 is negative, large, and peaked at a critical wave vector ζ_0, indicating a strong screening due to the electon-phonon coupling and Fermi-surface nesting. Both ζ_0 and the intensity of the anomaly are strongly dependent upon strain. The value of ζ_0 increases with decreasing c/a, the intensity reaching its maximum at $c/a = 0.97$.

V. SUMMARY AND CONCLUSIONS

Our *ab initio* study of the phonon dispersion and lattice instabilities in cubic and tetragonal Ni_2MnGa can be summarized as follows.

First, the parent cubic phase exhibits a marginal elastic instability, $C' \approx 0$, meaning that there is almost no energy cost for a small uniform tetragonal distortion.

Second, for $0.91 < c/a < 1.06$ a Kohn anomaly is present

due to electron-phonon coupling and Fermi-surface nesting. It develops into a deep minimum corresponding to a localized dynamical instability whose wave vector ζ_0 is related in a one-to-one fashion to the c/a ratio. Therefore, tetragonal structures with c/a in this range are unstable towards a particular transverse (110)-shuffling modulation with a specific wave vector ζ_0, the one-to-one relationship of the c/a ratio and the modulation period being due to the behavior of the topology of the Fermi surface under tetragonal distortions.

Consequently, the energy of the cubic structure may be lowered by any one of a family of deformations, $\{\epsilon, \mathbf{u}(\zeta_\epsilon)\}$, consisting of a tetragonal strain ϵ and a superimposed (110)-shuffling modulation, $\mathbf{u}(\zeta_\epsilon)$ whose periodicity ζ is directly related in a one-to-one fashion to the c/a ratio.

The near-vanishing of C' together with the fact that the energy surface as a function of c/a is remarkably flat permits a modulated ground state with c/a significantly different from 1. Indeed, the computed relation between c/a and the modulation wave vector is in excellent agreement with structural data on the premartensitic ($c/a=1$) and martensitic ($c/a=0.94$) phases of Ni_2MnGa, and also with the unmodulated stress-induced phase ($c/a=1.18$).

The next step is to carry out total-energy calculations of the complex modulated structures in order to determine the equilibrium amplitude and phase of the lattice modulation and the associated energy gain.[30] The energy could then be expanded in terms of symmetry invariants of the relevant structural degrees of freedom (strain and modulation) and determine the coefficients of each term of the expansion using *ab initio* calculations. In this way one could develop an *ab initio* based finite-temperature statistical model of the phase transition in Ni_2MnGa. This would also permit one to directly connect first-principles results with phenomenological Landau-theory parameters and obtain microscopic information about the transitions, such as the role of the magnetoelastic coupling in stabilizing the premartensitic phase.[31]

In conclusion, we have provided a first-principles microscopic explanation for the origin of the physically interesting and technologically important martensitic phase transitions in the ferromagnetic shape-memory Heusler alloy Ni_2MnGa.

ACKNOWLEDGMENTS

Calculations in this work have been done using the PWSCF package.[25] We thank Morrel Cohen, Richard James, and Xiangyang Huang for valuable discussions, and Vitaly Godlevsky for his help in the early stages of this work. This work was supported by AFOSR/MURI F49620-98-1-0433.

*Email address: bungaro@physics.rutgers.edu

[1] S.J. Murray, M.A. Marioni, A.M. Kukla, J. Robinson, R.C. O'Handley, and S.M. Allen, J. Appl. Phys. **87**, 5774 (2000).
[2] A. Sozinov, A.A. Likhachev, N. Lanska, and K. Ullakko, Appl. Phys. Lett. **80**, 1746 (2002).
[3] A. Zheludev, S.M. Shapiro, P. Wochner, A. Shwartz, M. Wall, and L.E. Tanner, Phys. Rev. B **51**, 11 310 (1995).
[4] A. Zheludev, S.M. Shapiro, P. Wochner, and L.E. Tanner, Phys. Rev. B **54**, 15 045 (1996).
[5] P.J. Webster, K.R.A. Ziebeck, S.L. Town, and M.S. Peak, Philos. Mag. **49**, 295 (1984).
[6] V.V. Martynov and V.V. Kokorin, J. Phys. III **2**, 739 (1992).
[7] R. Tickle and R.D. James, J. Magn. Magn. Mater. **195**, 627 (1999).
[8] V. Buchelnikov, A. Zayak, A. Vasilev, and T. Takagi, Int. J. Appl. Electromagn. Mech. **12**, 19 (2000).
[9] A. Dal Corso and S. de Gironcoli, Phys. Rev. B **62**, 273 (2000).
[10] A. Dal Corso, A. Pasquarello, and A. Baldereschi, Phys. Rev. B **56**, 11 369 (1997).
[11] D. Vanderbilt, Phys. Rev. B **41**, 7892 (1990).
[12] The details for the Ni pseudopotential can be found in Ref. 9.
[13] We generated the pseudopotential for Mn, using as reference the all-electron configuration $3d^5 4s^2$. The core radii are (in a.u.) $4s$ (2.0, 2.2), $4p$ (2.2, 2.4), $3d$ (1.6, 2.2). The all-electron potential pseudized inside $r_c=1.8$ has been taken as a local potential. Two values of the core radii indicate a channel which has been pseudized with the ultrasoft scheme. In such a case the first value is the norm-conserving core radius and the second is the ultrasoft one.
[14] S. Louie, S. Froyen, and M.L. Cohen, Phys. Rev. B **26**, 1738 (1982).
[15] J.P. Perdew, K. Burke, and M. Ernzerhof, Phys. Rev. Lett. **77**, 3865 (1996).
[16] M. Methfessel and A.T. Paxton, Phys. Rev. B **40**, 3616 (1989).
[17] H.J. Monkhorst and J.D. Pack, Phys. Rev. B **13**, 5188 (1976).
[18] S. Baroni, S. de Gironcoli, A. Dal Corso, and P. Giannozzi, Rev. Mod. Phys. **73**, 515 (2001).
[19] A. Ayuela, J. Enkovaara, K. Ullakko, and R.M. Nieminen, J. Phys.: Condens. Matter **11**, 2017 (1999).
[20] M. Pugaczowa-Michalska, Acta Phys. Pol. A **96**, 467 (1999).
[21] A. Zheludev, S.M. Shapiro, P. Wochner, A. Shwartz, M. Wall, and L.E. Tanner, J. Phys. IV **5**, C8-1139 (1995).
[22] Y. Lee, J.Y. Rhee, and B.N. Harmon, Phys. Rev. B **66**, 054424 (2002).
[23] O.I. Velikokhatny and I.I. Naumov, Phys. Solid State **41**, 617 (1999).
[24] O.H. Nielsen and R.M. Martin, Phys. Rev. B **32**, 3780 (1985); **32**, 3792 (1985).
[25] S. Baroni, A. Dal Corso, S. de Gironcoli, and P. Giannozzi, http://www.pwscf.org
[26] See Fig. 1 in V.V. Godlevsky and K.M. Rabe, Phys. Rev. B **63**, 134407 (2001).
[27] J. Worgull, E. Petti, and J. Trivisonno, Phys. Rev. B **54**, 15 695 (1996).
[28] L. Mañosa, A. Gonzàlez-Comas, E. Obradó, A. Planes, V.A. Chernenko, V.V. Kokorin, and E. Cesari, Phys. Rev. B **55**, 11 068 (1997).
[29] V.V. Martynov, J. Phys. IV **5**, C8-91 (1995).
[30] Results of calculations for the modulated structure with $c/a=0.94$ can be found in A.T. Zayak, P. Entel, J. Enkovaara, A. Ayuela, and R.M. Nieminen, J. Phys.: Condens. Matter **15**, 159 (2003).
[31] A. Planes, E. Obradó, A. Gonzàlez-Comas, and L. Mañosa, Phys. Rev. Lett. **79**, 3926 (1997).
[32] P.J. Webster, Contemp. Phys. **10**, 559 (1969).